Measuring the shock impedance mismatch between high-density carbon and deuterium at the National Ignition Facility

M. Millot,[1,*] P. M. Celliers,[1] P. A. Sterne,[1] L. X. Benedict,[1] A. A. Correa,[1] S. Hamel,[1] S. J. Ali,[1] K. L. Baker,[1] L. F. Berzak Hopkins,[1] J. Biener,[1] G. W. Collins,[1,2,3] F. Coppari,[1] L. Divol,[1] A. Fernandez-Panella,[1] D. E. Fratanduono,[1] S. W. Haan,[1] S. Le Pape,[1] N. B. Meezan,[1] A. S. Moore,[1] J. D. Moody,[1] J. E. Ralph,[1] J. S. Ross,[1] J. R. Rygg,[1,2] C. Thomas,[1] D. P. Turnbull,[1,2] C. Wild,[4] and J. H. Eggert[1]

[1]*Lawrence Livermore National Laboratory, Livermore, California 94550, USA*

[2]*Laboratory for Laser Energetics, University of Rochester, Rochester, New York 14623, USA*

[3]*Departments of Mechanical Engineering, and Physics and Astronomy, University of Rochester, Rochester, New York 14627, USA*

[4]*Diamond Materials GmbH, 79108 Freiburg, Germany*

(Received 14 November 2017; revised manuscript received 9 January 2018; published 18 April 2018)

Fine-grained diamond, or high-density carbon (HDC), is being used as an ablator for inertial confinement fusion (ICF) research at the National Ignition Facility (NIF). Accurate equation of state (EOS) knowledge over a wide range of phase space is critical in the design and analysis of integrated ICF experiments. Here, we report shock and release measurements of the shock impedance mismatch between HDC and liquid deuterium conducted during shock-timing experiments having a first shock in the ablator ranging between 8 and 14 Mbar. Using ultrafast Doppler imaging velocimetry to track the leading shock front, we characterize the shock velocity discontinuity upon the arrival of the shock at the HDC/liquid deuterium interface. Comparing the experimental data with tabular EOS models used to simulate integrated ICF experiments indicates the need for an improved multiphase EOS model for HDC in order to achieve a significant increase in neutron yield in indirect-driven ICF implosions with HDC ablators.

DOI: 10.1103/PhysRevB.97.144108

Plastic polymers (CH), beryllium, and carbon (diamond) are efficient ablators for laser-driven dynamic compression owing to their low atomic numbers and relatively high densities. Diamond is currently being used as an ablator in high-energy density (HED) experiments [1–3] at the Omega Laser Facility as well as in integrated experiments for inertial confinement fusion (ICF) research [4–8] at the National Ignition Facility (NIF), where its advantages contributed to achieving record nuclear fusion yield [9]. An extended knowledge of its equation of state (EOS) and transport properties at extreme densities, pressures, and temperatures is important to ensure the accuracy and predictability of the radiation-hydrodynamic simulations used to model integrated ICF experiments.

Diamond, the least compressible material at ambient conditions, has been extensively studied using various static and dynamic compression techniques. Its shock equation of state has been documented [10–15] to ∼25 Mbar along the locus of shock states (Hugoniot) and 50 Mbar with ramp compression [16,17]. A shock and release experimental study was also performed recently on single-crystal and nanocrystalline diamond (NCD) up to 26 Mbar [15]. In addition, the onset of significant optical reflectivity, i.e., metallicklike electrical conductivity, has been evidenced to occur simultaneously with the completion of melting along the Hugoniot [18,19] near $U_S = 25$ km/s.

Due to extremely challenging fabrication constraints, NIF capsule ablators are made of slightly underdense fine-grained (lateral crystallite dimension ∼1–3 μm) polycrystalline diamond [20,21], usually referred to, in ICF research, as high-density carbon (HDC) with densities ranging from 94% to 99% of the density of single-crystal diamond (3.51 g/cm^3). Experimental data on the high pressure–high temperature properties of this material are lacking, so that diamond EOS models are used in pre- and postshot radiation-hydrodynamic simulations. Note that the targets for the ramp compression experiments of Ref. [17] were not made of full-density diamond. Instead, the synthetic diamond material had a layered microstructure with alternating 0.35-μm-thick layers of very fine 20-nm grains and layers of larger ∼350-nm grains with an average density of ∼3.25 g/cm^3 [21]. Similarly, the NCD material studied in Ref. [15] has a significantly lower density (3.37 g/cm^3) than the HDC currently used in ICF implosion capsules ($\rho \sim 3.44$–3.48 g/cm^3), because, in similar synthesis conditions, the microstructure of the obtained HDC material is affected by the curvature of the spherical shells and cannot be replicated in planar *foils*.

Here, we report shock and release measurements between HDC and cryogenic liquid deuterium using the shock-timing *keyhole* platform at the NIF [22,23] [Fig. 1(a)]. Our approach is similar to the work of Ref. [24], aimed at measuring the shock impedance mismatch between glow discharge polymer (GDP) and D_2 and provides experimental benchmarks for the existing tabular equation of state models for HDC and D_2, in particular, on the shock and release behavior in the vicinity of the melting line near 10 Mbar. The experimental data suggest that the current EOS tabular models need to be improved to accurately describe the shock impedance mismatch between HDC and D_2.

*millot1@llnl.gov

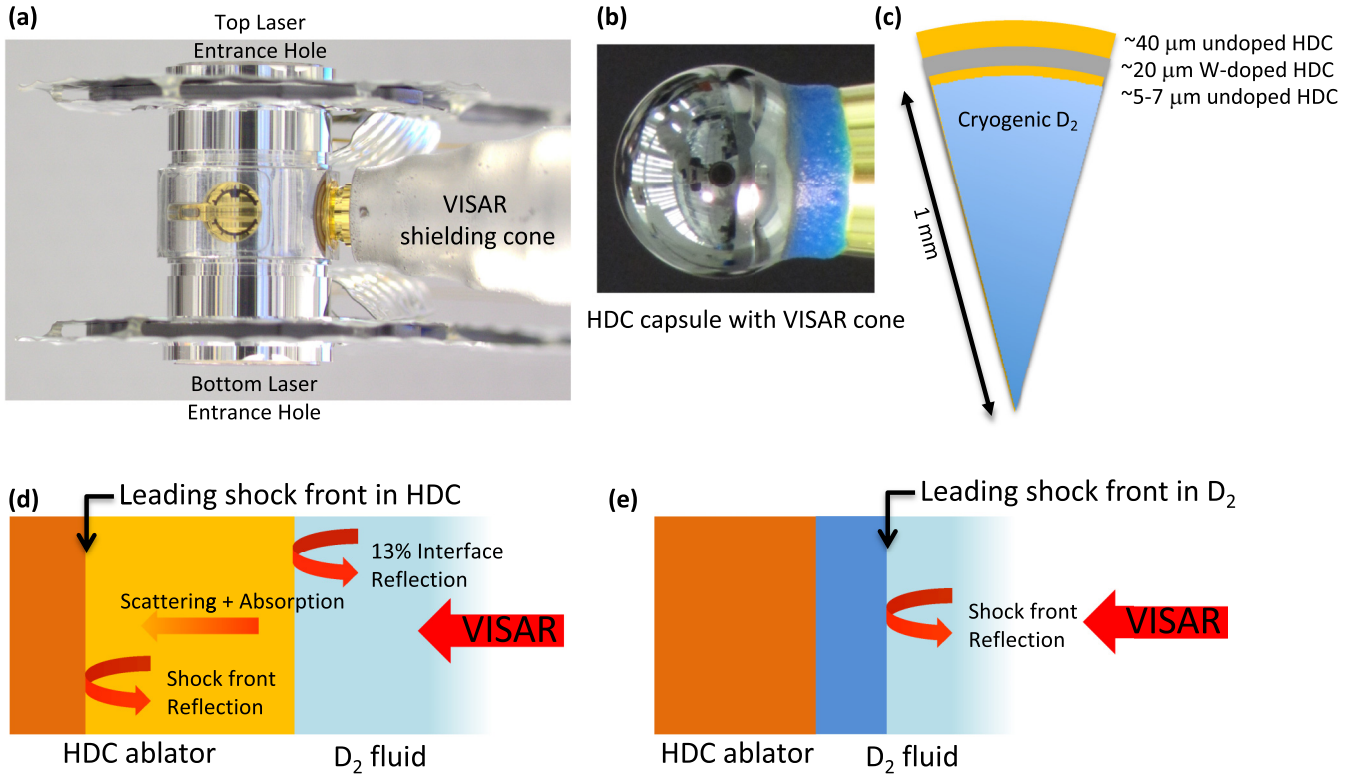

FIG. 1. Experimental concept. (a)–(c) Keyhole targets [22,24–26] containing high-density carbon (HDC) capsules filled with liquid deuterium are indirectly driven using up to 192 beams at the National Ignition Facility (NIF) pointed at the top and bottom laser entrance holes. Most recent W-doped capsules have a multishell structure with the innermost 5 μm made of undoped HDC with $\rho \sim 3.44$ g/cm^3, a W-doped layer, an undoped HDC outer layer with $\rho \sim 3.48$ g/cm^3, and a 3-μm-thick nanocrystalline undoped HDC topcoat with $\rho \sim 3.30$ g/cm^3. The density of the W-doped layer depends on the doping level, from 3.56 g/cm^3 with 0.16 at. % W to 3.60 g/cm^3 with 0.25 at. % W and 3.64 g/cm^3 with 0.33 at. % W. An accurately shaped, 5–7 ns long pulse launches a series of strong shock waves into the capsule. Using a gold cone inserted in the capsule and sealed by a transparent window, the interferometric Doppler velocimeter VISAR instrument [27] tracks the shock velocity history inside the ablator and the deuterium. (d) Observing the shock velocity inside the HDC capsule is challenging because of scattering due to its microstructure, absorption due to photoionization, strong Fresnel reflection at the interface, and weak reflection at the shock front below 25 km/s. (e) Once the shock has reached the fluid D_2, it is easily tracked with VISAR to measure its shock velocity up to 150 km/s.

Shock-timing experiments with cryogenic liquid deuterium as a surrogate for the deuterium-tritium ice fusion fuel [7,8,22,25,26] are essential to the ICF effort at NIF as they allow us to accurately benchmark integrated implosion simulations at the early time. In these experiments, precisely shaped, 5–7 ns long drive-laser pulses are used to launch a series of shocks into the ablator. We use the *keyhole* platform (Fig. 1) with a gold cone inserted in the HDC spherical capsule and sealed by a transparent window to allow a line of sight for the two-channel, ultrafast, line-imaging velocimetry interferometer system for any reflector (VISAR) inside the capsule [27]. When shocked to sufficiently high pressure, diamond and deuterium both become optically reflecting, allowing VISAR to directly track the velocity of the shock front to establish the compression sequence. In addition, inserting one or more mirrors in the gold cone allows one to gain insight into the implosion symmetry by comparing the shock sequence along multiple directions [28,29].

Observing the initial shock before it breaks out of the HDC capsule and into the liquid deuterium fill presents several challenges (Fig. 1). Due to the absence of an antireflection coating, the large refractive index mismatch generates a strong Fresnel reflection of the VISAR laser probe at the HDC/D_2 interface. With $n(\mathrm{HDC}) \simeq 2.40$ and $n(D_2) \simeq 1.14$, the interface reflectivity is $R = |n(\mathrm{HDC}) - n(D_2)|^2/|n(\mathrm{HDC}) + n(D_2)|^2 \simeq 13\%$. In addition, the fine-grained structure of HDC induces significant incoherent light scattering: Thick fine-grained HDC layers appear opaque. HDC can also become opaque due to the absorption of hot electrons [30] and/or x rays generated during the laser plasma interactions inside the hohlraum (blanking). These two effects combine to severely attenuate the propagation of the VISAR laser probe deep into the HDC layer.

Finally, the shock front reflectivity in HDC can be as low as a few percent or less at the lowest pressure range explored in the NIF keyhole experiments. Direct measurements are lacking, but we can estimate that the reflectivity of shocked HDC will rise quickly with increasing shock velocity, similarly to the reported behavior for full-density diamond [18,19] when shocked into the liquid phase. For reference, the reflectivity of diamond increases from ~1% at 21 km/s to saturation near ~30% above 25 km/s. We can therefore expect to observe a similar rapid onset of shock reflectivity at the same or possibly slightly lower shock velocity, since being 1%–5% underdense, HDC will reach slightly higher shock temperatures than diamond.

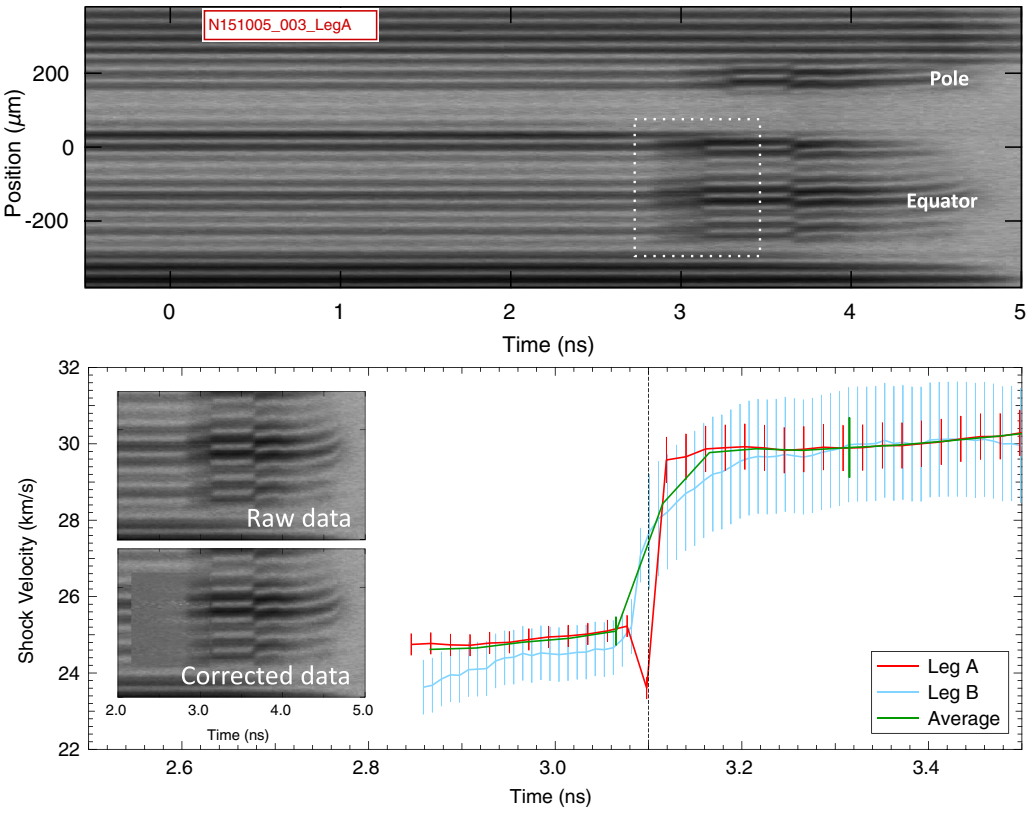

FIG. 2. Experimental VISAR data and inferred shock velocity. Top: Example VISAR record for a two-axis keyhole experiment with an HDC ablator. Bottom: Corresponding shock velocity along the equator in the HDC ($t < 3.1$ ns) and in the D_2 ($t > 3.1$ ns) showing the sudden acceleration of the shock as it is transmitted into the deuterium (near 3.1 ns, vertical dotted line), including a weighted average of the velocity histories from VISAR channels leg A and leg B. Inset: Raw data for the equator region before and after ghost fringe subtraction [3].

When VISAR is used to monitor the velocity of reflecting shock fronts in a given medium at rest, the observed fringe shift is proportional to the apparent velocity $U_{S,\mathrm{app}}$ of a fictional mirror moving into vacuum. It can be shown [27] that $U_{S,\mathrm{app}}$ is the product of the true shock velocity U_S and the index of refraction n of the unshocked medium at the VISAR wavelength (here, 659.5 nm) so that $U_S = U_{S,\mathrm{app}}/n$.

Figure 2 shows an example VISAR record for one of these experiments showing the shock velocity discontinuity due to shock impedance mismatch between HDC and the liquid deuterium. Optimized high-Z doping in the capsules successfully mitigated blanking issues and allowed the collection of VISAR patterns clearly exhibiting fringe motion due to reflection at the shock front in HDC. Before 2.8 ns, VISAR only records the static *ghost fringes* due to the Fresnel reflection at the HDC/D_2 interface. Near 2.8 ns, the fringe contrast suddenly changes. This indicates the superposition of an additional fringe pattern due to the reflection of the VISAR probe at the shock front in the HDC ablator. A simple algorithm [3] can be used to eliminate the ghost fringes due to the Fresnel reflection at the ablator/fuel interface and isolate the signal carrying the information on the HDC shock velocity (inset of Fig. 2). Retrieving the fringe phase and using the two channels with different sensitivities, we obtain the shock velocity history $U_S(t)$ (bottom of Fig. 2) showing the sudden acceleration of the shock as it is transmitted into the deuterium. Linear fits of $U_S(t)$ over ~200 ps before and after breakout provide the velocities at breakout for both legs A and B. The weighted averages of these velocities, accounting for higher sensitivity in leg A, yield U_S(HDC) and $U_S(D_2)$.

Using the Rankine-Hugoniot equations and tabular EOS models for HDC and D_2, one can compute the expected change in shock velocity at the interface between the HDC ablator and the liquid D_2 resulting from the shock impedance mismatch between these two media by an impedance-matching procedure [34,35] (see Fig. 3). As the HDC ablator is first shock compressed and then released to ensure the continuity of the pressure and particle velocity at the interface [34,35], the predicted U_S(HDC)-$U_S(D_2)$ for a given model therefore depends on both the shock and release behaviors as illustrated in Fig. 3.

Figure 4 shows most high-pressure experimental shock data previously collected at large laser [10–12] and pulse-power [13] facilities along with calculated theoretical Hugoniot curves. Below 500 GPa (5 Mbar), most current tabular EOS models predict very similar shock compressibility, likely because they were fit to the same data in this range, well below melting. Above 500 GPa, as shown in Fig. 4, theoretical Hugoniot curves rapidly span a much broader region of the pressure-density space. Near 12 Mbar, LLNL 9069 (similar to LANL 7834) and LLNL 65/64 predict a much stiffer response, with densities near 6.8 g/cm^3 compared to 7.4 g/cm^3 according to LLNL 9061 and LANL Sesame 7830. The high accuracy data from Refs. [12,13] are in agreement and suggest that the stiffer models are not valid in the 6–20 Mbar range.

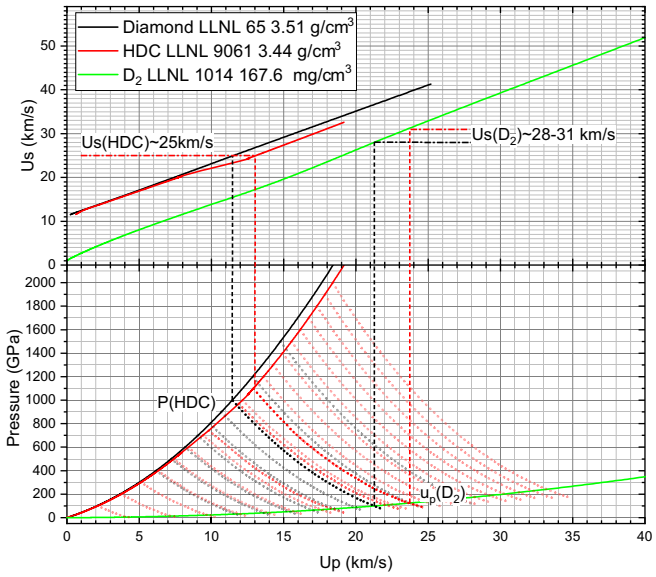

FIG. 3. Graphical construction of the impedance-matching procedure. Calculated Hugoniot curves are shown in U_S-u_p and P-u_p spaces (solid lines), together with calculated isentropic release curves (dotted lines). For a given incident velocity U_S(HDC), one can determine, for a given HDC EOS, the incident particle velocity in HDC, u_p(HDC), using the top panel, then follow a vertical line at constant u_p to the lower panel to determine the incident shock pressure P(HDC). Then, following a release curve until it crosses the D_2 Hugoniot, one determines the approximate transmitted shock pressure $P(D_2)$ and particle velocity $u_p(D_2)$. Following again a vertical, constant u_p line back up into the upper panel until the intersection with the deuterium U_S-u_p Hugoniot line, one obtains an approximate transmitted shock velocity $U_S(D_2)$. Dashed-dotted and dashed lines show that for a given incident shock velocity $U_S(\text{HDC}) = 25$ km/s, LLNL 65 and 9061 models predict two very different transmitted shock velocities $U_S(D_2)$ respectively near 28 and 31 km/s.

The results from 15 different shock-timing experiments at the NIF are shown in Fig. 5 (blue squares). These experiments provide 28 sets of velocities tracked either along the equatorial or the polar direction, together with the predicted velocity jump between HDC and D_2 for several different EOS models. Strong variations between the model predictions are noticeable. Figure 5 also indicates that no EOS model matches the experimental data over the explored velocity range between ~23 and ~27 km/s corresponding to ~8–14 Mbar. In particular, a strong discrepancy is found between the data and the most detailed and recent EOS model to date [36] (LLNL 9061). In contrast, the LLNL 9069 model seems to match the data the best, but this is the result of the cancellation of errors in the P-up plane, including the dramatically too stiff response along the principal Hugoniot illustrated in Fig. 4.

An important parameter of the calculations is the description of the shock compressibility of deuterium. As with most simulations of ICF research experiments at NIF, we used primarily LLNL 1014 (based on Kerley's 2003 model [32]). Since several experiments suggest that the compressibility of shocked deuterium in the regime of interest for ICF implosions might be slightly higher than predicted [35,37–39] by LLNL 1014, we also computed the predicted shock velocity jumps using a recent model constructed using density functional

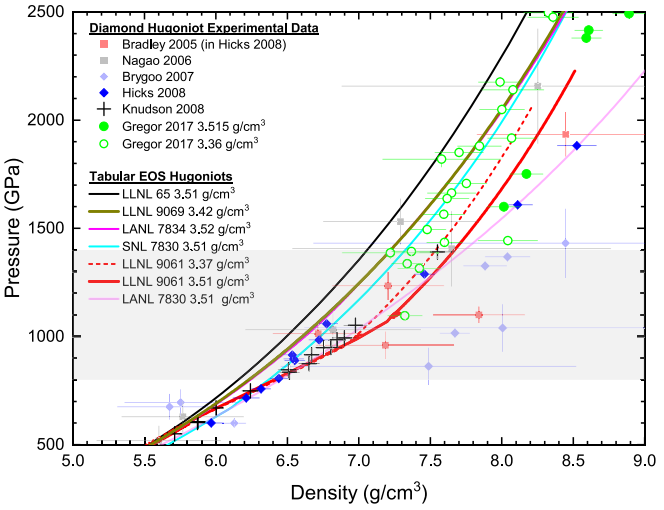

FIG. 4. Diamond Hugoniot: Experimental data and tabular EOS models. The gray shaded area indicates the pressure range of the shock states explored in the present experiments. Data from Refs. [11,12] measured relative to a quartz standard, and the data from Ref. [10] and Bradley *et al.* [12] using an Al standard were reanalyzed using updated quartz and Al Hugoniot models [31]. Reference [13] used a Cu standard. Data from Ref. [15] collected with a quartz standard are also included.

theory based molecular dynamics (DFT-MD) simulations [33] (dashed lines in Fig. 5) that is found to correctly capture the P-ρ behavior of shocked D_2. However, this does not bring the data into agreement with LLNL 9061.

We verified that the discrepancy in shock velocity jump was not due to uncertainty in the refractive index n of the HDC

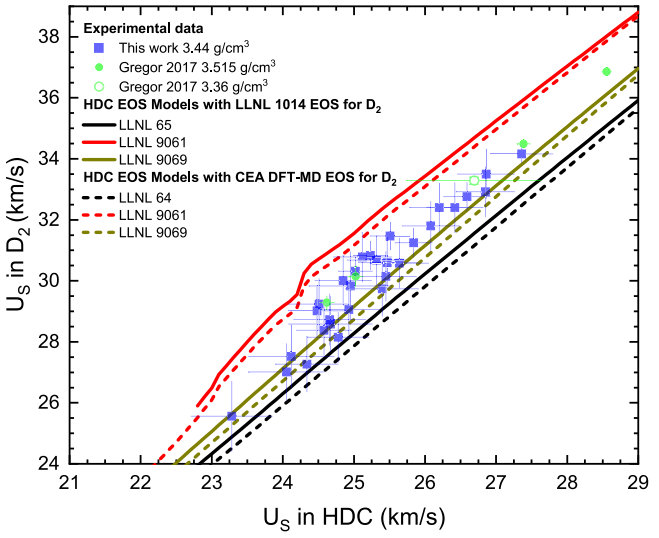

FIG. 5. Shock velocity jump at the interface between the HDC ablator and the liquid D_2 fuel surrogate. Experimental data (blue squares) assuming 2.40 as the refractive index of unshocked HDC. Calculated velocity jumps for various HDC EOS models assuming LLNL 1014 (based on Kerley's 2003 model [32], solid lines) or the DFT-MD based CEA table [33] (dashed lines) as the deuterium EOS with an initial density $\rho_0 = 168$ mg/cm^3. Data from Ref. [15] are also included.

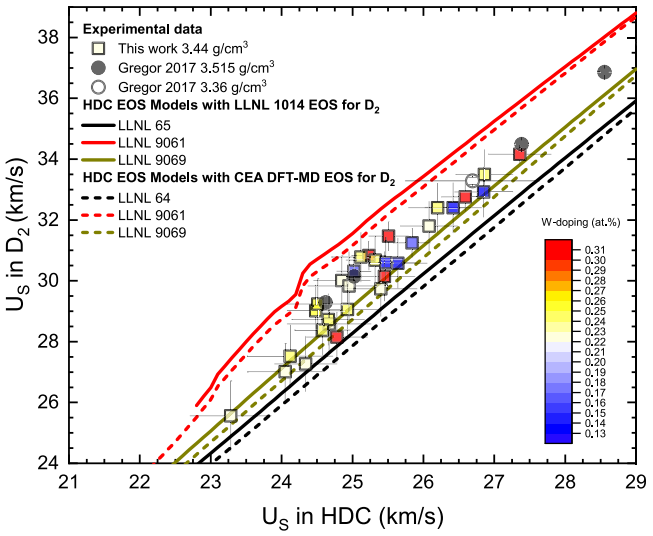

FIG. 6. Influence of W doping on the shock impedance mismatch. Same data as reported in Fig. 5 with the level of W doping as a color code. One could expect that increasing the W-doping level should contribute to mitigating the photoionization and/or preheat effects. No clear correlation appears between the level of doping and the disagreement between the data and the 9061 model.

as the primary observable in our experiment is the apparent velocity $U_{S,\mathrm{app}}$ from which we extract the shock velocity U_S using $U_S = U_{S,\mathrm{app}}/n$ (see Appendix A).

An unexpected significant preheat can also be ruled out since calculations (not shown) considering either preheated deuterium, or preheated HDC, as well as the case of preheat in the two materials further enhances the discrepancy in impedance mismatch shown in Fig. 5. Note that no early fringe motion is detected on the VISAR records, suggesting the absence of a significant preheat near the ablator/fuel interface. Figure 6 also shows no clear correlation between the level of W doping and the disagreement between the data and the 9061 model. As one could expect that increasing the W-doping level should mitigate the photoionization and/or preheat effects, the absence of correlation suggests that either preheat/photoionization effects are negligible or the doping variations are too small to matter.

The large discrepancy between the experimental $U_S(\mathrm{D_2})$-$U_S(\mathrm{HDC})$ values and the predicted curves with LLNL 9061 suggests that this model, which accurately described the shock compressibility, fails to correctly capture the release behavior of HDC. To investigate whether this discrepancy was caused by the parametrization of the EOS, we computed the impedance-matching $U_S(\mathrm{D_2})$-$U_S(\mathrm{HDC})$ curves directly using the pressure and internal energy values obtained from the DFT-MD simulations that were used [36] to fit the broad range analytical free-energy model for the LLNL 9061 table. This does not provide a better agreement between the experimental shock velocity jump and the predicted ones. Similarly, slight modifications of the liquid free energy of 9061 aimed at appeasing agreement with both the melt temperature and the specific heat inferred in Ref. [19] do not lift the discrepancy. It is therefore possible that the *ab initio* calculations, as performed, used to constrain 9061 [36], lack accuracy in the low-ρ, high-T regimes of importance for impedance matching with deuterium.

Previous shock temperature measurements [19] showed that melting starts near 7–8 Mbar and is complete near 10 Mbar along the diamond Hugoniot. Since theoretical simulations [40] suggest a negative Clapeyron slope near 7–10 Mbar, release isentropes from shock states right above 10 Mbar might cross the melting line, causing nontrivial release behavior including kinetic effects. Indeed, an increase in the scatter of the $U_S(\mathrm{D_2})$-$U_S(\mathrm{HDC})$ data, perhaps even suggesting a break in the slope, appears in Fig. 5 near $U_S(\mathrm{HDC}) = 25$ km/s (10 Mbar). Such a scenario could have dramatic implications in the ICF implosion context as it could significantly affect the roughness of the shock front both in physical and in velocity space and seed hydrodynamic instabilities at the ablator/fuel interface. Further investigations also include testing the influence of the exchange correlation functional on the DFT-MD calculations, in particular, at the lowest densities for which experimental data are lacking.

ACKNOWLEDGMENT

This work was prepared by LLNL under Contract No. DE-AC52-07NA27344.

APPENDIX A: EXPERIMENTAL DETAILS

The velocity resolution of the VISAR for the HDC/$\mathrm{D_2}$ impedance match event is somehow limited because the fused silica étalons were selected to allow tracking the subsequent shocks in the deuterium fluid traveling much faster, up to 150 km/s. Most shots used 4.5799 mm on leg A and 1.8332 mm on leg B, giving a vacuum velocity per fringe (vvpf) of 13.635 and 34.065 km/s/fringe, while others used 8.006 and 3.2196 mm, yielding vvpf of 7.8001 and 19.296 km/s/fringe. Taking into account the ability to resolve the fringe phase and accounting for the discrepancies between the two legs, the velocity resolution for most shots was ∼5% of a fringe for the most resolving étalon, that is, ∼0.28 km/s in HDC and 0.60 km/s in $\mathrm{D_2}$.

At the conditions of the experiments, $T = 21.5$ K and $P \sim 800$ Torr, the refractive index of deuterium at 660 nm is [24] $n(\mathrm{D_2}) = 1.136$ and the initial density is $\rho_0(\mathrm{D_2}) = 168$ mg/cm^3.

The shock velocity measurements reported here are conducted when the shock wave is in the innermost HDC layer with density near 3.44 g/cm^3. Published data on the refractive index on this fine-grained HDC capsule material are lacking, but preliminary characterization measurements on 8-μm-thick layers of undoped HDC grown under the same conditions as the capsules used in the experiments reported here indicated $n \simeq 2.35$–2.40 at 660 nm, in agreement with previously published data for nanocrystalline diamond with a similar density [41–44].

The analyses reported in all figures assumed $n = 2.40$. This appears as a conservative choice because as the actual shock velocity is given by $U_S = U_{\mathrm{app}}/n$, one would need to assume a *higher* index for HDC in order to reconcile the predictions using LLNL 9061 and the experimental data in Fig. 5. A quick estimate brings the *necessary* index to be around 2.50.

TABLE I. Reanalyzed diamond Hugoniot equation of state data.

Shot ID	Standard	ρ_0 (g/cm^3)	U_S (km/s)	u_p (km/s)	P (GPa)	ρ (g/cm^3)	Source
26332	Al	3.51	29.00 ± 1.16	15.04 ± 1.03	1530.78 ± 104.88	7.29 ± 0.54	Nagao
26396	Al	3.51	19.90 ± 0.86	7.43 ± 0.96	518.91 ± 67.32	5.60 ± 0.43	Nagao
27300	Al	3.51	32.70 ± 1.70	18.79 ± 2.31	2156.99 ± 264.62	8.25 ± 1.37	Nagao
28693	Al	3.51	27.20 ± 1.44	14.72 ± 1.81	1405.35 ± 173.13	7.65 ± 1.11	Nagao
28695	Al	3.51	21.40 ± 1.33	8.38 ± 0.96	629.38 ± 72.15	5.77 ± 0.43	Nagao
28697	Al	3.51	24.60 ± 2.29	11.94 ± 1.14	1031.01 ± 98.41	6.82 ± 0.61	Nagao
20547	Al	3.51	23.12 ± 0.34	11.83 ± 0.75	959.69 ± 61.17	7.19 ± 0.48	Bradley
24278	Al	3.51	24.58 ± 0.26	11.73 ± 0.60	1012.34 ± 52.16	6.72 ± 0.32	Bradley
24365	Al	3.51	23.82 ± 0.26	13.16 ± 0.43	1100.03 ± 36.36	7.84 ± 0.32	Bradley
24294	Al	3.51	26.18 ± 0.26	13.43 ± 0.69	1233.69 ± 63.43	7.20 ± 0.39	Bradley
24288	Al	3.51	30.70 ± 0.27	17.95 ± 0.94	1933.79 ± 100.89	8.45 ± 0.62	Bradley
20541	Al	3.51	34.95 ± 0.35	23.86 ± 1.82	2926.57 ± 222.95	11.06 ± 1.81	Bradley
26397	Mo	3.51	39.08 ± 0.33	26.10 ± 1.42	3580.00 ± 192.10	10.57 ± 1.17	Bradley
49976	Quartz	3.51	20.39 ± 0.24	8.39 ± 0.12	600.72 ± 8.84	5.97 ± 0.09	Hicks
50364	Quartz	3.51	21.66 ± 0.13	9.42 ± 0.16	716.30 ± 12.45	6.21 ± 0.09	Hicks
49974	Quartz	3.51	22.05 ± 0.11	9.80 ± 0.11	758.30 ± 8.58	6.32 ± 0.07	Hicks
49614	Quartz	3.51	22.46 ± 0.08	10.22 ± 0.11	805.62 ± 8.66	6.44 ± 0.06	Hicks
51565	Quartz	3.51	23.36 ± 0.07	10.84 ± 0.13	889.11 ± 10.50	6.55 ± 0.07	Hicks
49616	Quartz	3.51	23.46 ± 0.07	10.88 ± 0.13	895.67 ± 10.55	6.54 ± 0.07	Hicks
49615	Quartz	3.51	23.72 ± 0.07	10.98 ± 0.12	914.11 ± 10.29	6.53 ± 0.07	Hicks
48882	Quartz	3.51	24.22 ± 0.07	11.57 ± 0.13	983.96 ± 10.83	6.72 ± 0.07	Hicks
48448	Quartz	3.51	25.02 ± 0.09	12.06 ± 0.14	1058.95 ± 12.42	6.78 ± 0.08	Hicks
48880	Quartz	3.51	26.33 ± 0.07	13.94 ± 0.11	1288.34 ± 10.16	7.46 ± 0.07	Hicks
49450	Quartz	3.51	28.42 ± 0.08	16.12 ± 0.15	1608.03 ± 14.92	8.11 ± 0.11	Hicks
49447	Quartz	3.51	30.19 ± 0.09	17.76 ± 0.19	1881.81 ± 19.72	8.53 ± 0.14	Hicks
B1	Quartz	3.51	26.30 ± 0.10	14.82 ± 0.21	1367.7600 ± 19.63	8.04 ± 0.16	Brygoo
B2	Quartz	3.51	20.00 ± 0.20	8.54 ± 0.10	599.7220 ± 7.60	6.13 ± 0.08	Brygoo
B3	Quartz	3.51	23.10 ± 0.10	12.53 ± 0.12	1016.1300 ± 10.29	7.67 ± 0.10	Brygoo
B4	Quartz	3.51	26.10 ± 0.10	14.48 ± 0.21	1326.2400 ± 19.46	7.88 ± 0.15	Brygoo
B5	Quartz	3.51	22.60 ± 1.00	8.77 ± 0.73	695.6390 ± 59.41	5.75 ± 0.39	Brygoo
B6	Quartz	3.51	23.10 ± 1.00	12.83 ± 1.33	1039.5500 ± 109.86	8.01 ± 1.39	Brygoo
B7	Quartz	3.51	26.60 ± 1.30	15.33 ± 1.65	1431.3200 ± 157.89	8.45 ± 1.76	Brygoo
B8	Quartz	3.51	21.60 ± 0.90	11.38 ± 1.10	862.5260 ± 84.81	7.49 ± 1.03	Brygoo
B9	Quartz	3.51	22.50 ± 0.90	8.55 ± 0.73	674.8500 ± 58.58	5.68 ± 0.36	Brygoo

Note that the cryogenic temperature required for the liquid deuterium does not affect the HDC refractive index. The temperature dependence of the far-infrared refractive index of diamond has been measured both optically [45] and electrically [46]: The index increases very slowly with temperature, by less than 0.001 between 21.5 and 300 K where most optical measurements are performed.

Modifications of the refractive index of the unshocked material ahead of the shock front by ablation-generated x rays have been reported but found to cause a small (0.001) decrease of the diamond real part of the refractive index [47], so that it is unlikely that this could be the cause for the discrepancy in shock velocity jump between the experiment and the models (Fig. 5).

APPENDIX B: REANALYSIS OF PREVIOUS DIAMOND HUGONIOT EQUATION OF STATE DATA

Most high-pressure Hugoniot equation of state measurements for diamond were performed relative to a standard using an impedance-matching procedure [34]. As the knowledge about standards is improved, reanalyzing the existing data is necessary and provides more accurate and precise data than the original analysis. All the data from Ref. [10], and four shots reported in Ref. [12] (from an unpublished study by Bradley *et al.*), used an aluminum standard. Reanalyzed data using the latest fit to high-precision aluminum Hugoniot data [31,34] are reported in Fig. 4 and Table I. The bulk of the data from Ref. [12] and the measurements from Ref. [11] were performed with a quartz standard and therefore reanalyzed using the constant Grüneisen reshock model in Ref. [12] and a fit of all available data for quartz shocked into the liquid phase for the quartz Hugoniot [35].

APPENDIX C: CURRENT TABULAR EQUATIONS OF STATE FOR DIAMOND

The available tabular EOS for modeling ICF implosions with HDC ablators are designed to describe full-density diamond, including the Lawrence Livermore National Laboratory

TABLE II. Diamond and HDC tabular equation of state models commonly used for ICF research.

Table	ρ_0 (g/cm^3)	Date	Multiphase	Comments
LANL Sesame 7830	3.51	1982	No	Very coarse temperature grid.
LLNL 65	3.51	1999	No	Poor fit to cold curve data.
SNL Sesame 7830	2.20	2001	Yes	Multicomponent and multiphase. Graphite initial state.
LANL Sesame 7834	3.51	2007	No	Fit to DFT-MD and Hugoniot [13] data. No attempt to accurately fit the melt region.
LLNL 9067	3.51	2007	Yes	Total functions P_t, E_t based on DFT-MD. Cold and thermal functions P_c, P_e, and P_i based on QEOS. P_t does not equal $P_c + P_e + P_i$.
LLNL 64	3.51	2007	No	Postdates L9067, but uses cruder EOS models for solid/melt region. Same as LLNL 65 along the Hugoniot.
LLNL 9061	3.37	2014	Yes	Best available EOS based on DFT-MD [36] and a range of experimental data.
LLNL 9069	3.42	2015	Yes	Same as the LLNL 9067 cold, ion-thermal, and electron-thermal terms.

(LLNL) multiphase model No. 9061 (Benedict/Correa/Sterne 2014) (see Table II). This EOS is based entirely on DFT and quantum Monte Carlo *ab initio* electronic structure calculations. The exchange-correlation functional used in the DFT [Perdew-Burke-Ernzerhof (PBE)] renders the equilibrium density at 300 K for the model, 3.456 g/cm^3, to be slightly less than the experimental value for full-density diamond (3.51 g/cm^3). It is therefore ∼2.5% higher than the measured value for HDC (3.37 g/cm^3). However, when we use the 9061 model in this work, we force the initial density in the principal Hugoniot calculation to be $\rho_0 = 3.37$ g/cm^3, producing the red curves in Figs. 3 and 4 (and likewise for the further analysis pertaining to the impedance matching with deuterium, shown in Fig. 5). The noticeable difference between the principal Hugoniot of 9061 and that of the other models, for states in the liquid ($P > 1000$ GPa; see Fig. 3), is not due to these small differences in the tables' ρ_0 values, but is rather due to the specific construction of the liquid free energy, described in Ref. [36].

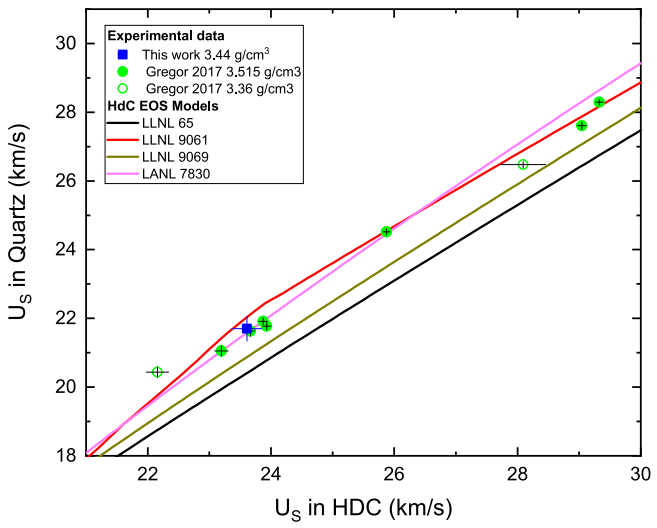

FIG. 7. Shock velocity jump at the interface between a CVD diamond slab and a quartz plate. Experimental data and predictions using various models for HDC and a fit to experimental data for the quartz Hugoniot [31]. Data from Ref. [15] are also included.

Previous diamond EOS tables include Los Alamos National Laboratory (LANL) Sesame 7830 (Bennett 1982) and 7834 (Crockett 2007), and LLNL 65 (LLNL 1999), 64 (LLNL 2007). LLNL 9069 is a quotidian EOS (QEOS) table constructed to match the multiphase table 9067 [48] (Correa/Benedict/Young 2007). LANL Sesame 7834 was fit to DFT-MD results and experimental Hugoniot data [13], but no attempt to accurately fit the melt region was made, in contrast to the explicitly multiphase LLNL 9067 and 9061 tables. Sandia National Laboratory (SNL) Sesame 7830 is a multicomponent and multiphase table for carbon (graphite is the reference state) built with the code PANDA (Kerley/Chhabildas) [49].

APPENDIX D: SHOCK AND RELEASE EXPERIMENTS BETWEEN HDC AND QUARTZ

We also report in Fig. 7 and Table III the result of a planar, impedance-matching event between a transparent slab of chemical vapor deposition (CVD) grown HDC and a z-cut α-quartz plate. This datum was obtained using data collected at the NIF to characterize drive conditions for proton-stopping power experiments [50]. We used $\rho_0 = 3.493$ g/cm^3, n[HDC](660 nm) = 2.41 [51], and n[quartz](660 nm) = 1.517 [52]. Using the LLNL 9061 model, the incident shock pressure in the CVD diamond slab was about 9 Mbar.

In addition to one new experimental datum for the shock impedance mismatch between CVD diamond and quartz, we report in Fig. 7 the prediction using various EOS models for HDC and a fit to high-precision experimental data [31]. Similar to the observation for the single shock states above, only LLNL 9061 and LANL Sesame 7830 models match well the experimental datum. Since the pressure drop at the diamond/quartz is only ∼30%, the release wave into the

TABLE III. Experimental details and result summary for a HDC/quartz shock impedance-matching experiment. The target package details with thicknesses in microns are Al[0.2]HDC[28]Au[2]HDC[492]quartz[525].).

Shot ID	U_S(HDC)	U_S(quartz)
N151214-003	23.61 ± 0.24	21.70 ± 0.36

TABLE IV. Experimental details and result summary for HDC/D_2 shock impedance-matching including details on the capsule ablator batch number, tungsten doping level, and calculated density of the doped layer. NYYMMDD-#-E and -P correspond to the data collected on shot NYYMMDD-# along the equator and polar direction, respectively.

Data set ID	U_S(HDC) (km/s)	U_S(D_2) (km/s)	Batch	W doping (at. %)	Density (g/cm^3)
N151004-005-E	25.40 ± 0.51	29.74 ± 0.90	KC038	0.22	3.59
N151004-005-E	24.34 ± 0.44	27.27 ± 0.91	KC038	0.22	3.59
N151005-003-P	24.05 ± 0.53	27.01 ± 0.93	KC038	0.22	3.59
N151101-001-E	24.67 ± 0.59	28.58 ± 0.91	KC038	0.22	3.59
N151101-001-E	23.28 ± 0.57	25.56 ± 1.15	KC038	0.22	3.59
N160110-002-E	26.08 ± 0.40	31.80 ± 0.81	KC038	0.22	3.59
N160114-003-E	24.85 ± 0.40	30.01 ± 0.81	KC038	0.22	3.59
N160114-003-P	24.95 ± 0.58	29.83 ± 1.12	KC038	0.22	3.59
N160131-001-E	26.86 ± 0.40	33.50 ± 0.81	KC047	0.24	3.60
N160131-001-P	26.20 ± 0.41	32.40 ± 0.80	KC047	0.24	3.60
N160419-001-E	25.51 ± 0.28	31.47 ± 0.47	K252	0.31	3.63
N160419-001-P	25.23 ± 0.24	30.83 ± 0.47	K252	0.31	3.63
N160523-001-E	24.66 ± 0.51	28.73 ± 0.84	KC047	0.24	3.60
N160523-001-P	24.12 ± 0.60	27.52 ± 1.03	KC047	0.24	3.60
N160724-005-E	25.12 ± 0.41	30.78 ± 0.81	KC047	0.24	3.60
N160724-005-P	25.32 ± 0.41	30.68 ± 0.81	KC047	0.24	3.60
N161115-002-E	24.58 ± 0.39	28.38 ± 0.82	KC047	0.24	3.60
N161115-002-P	24.93 ± 0.43	29.06 ± 0.82	KC047	0.24	3.60
N170119-001-E	25.02 ± 0.24	30.32 ± 0.46	KC206	0.16	3.56
N170119-001-P	25.84 ± 0.26	31.25 ± 0.47	KC206	0.16	3.56
N170228-002-E	25.47 ± 0.41	30.60 ± 0.82	KC210	0.13	3.55
N170228-002-P	25.64 ± 0.41	30.58 ± 0.82	KC210	0.13	3.55
N170409-002-E	26.42 ± 0.40	32.40 ± 0.82	KC210	0.13	3.55
N170409-002-P	26.85 ± 0.41	32.92 ± 0.82	KC210	0.13	3.55
N170809-001-E	24.78 ± 0.43	28.15 ± 0.82	K252	0.31	3.63
N170809-001-P	25.45 ± 0.43	30.15 ± 0.81	K252	0.31	3.63
N171016-002-E	24.48 ± 0.40	29.02 ± 0.84	KC245	0.25	3.60
N171016-002-P	24.51 ± 0.43	29.24 ± 0.83	KC245	0.25	3.60

diamond ablator does not lower the density too much and it is not too surprising that the model which describes well single shock states manages to capture this behavior as well. (See Table IV.)

[1] D. E. Fratanduono, T. R. Boehly, M. A. Barrios, D. D. Meyerhofer, J. H. Eggert, R. F. Smith, D. G. Hicks, P. M. Celliers, D. G. Braun, and G. W. Collins, J. Appl. Phys. **109**, 123521 (2011).

[2] F. Coppari, R. F. Smith, J. H. Eggert, J. Wang, J. R. Rygg, A. Lazicki, J. A. Hawreliak, G. W. Collins, and T. S. Duffy, Nat. Geosci. **6**, 926 (2013).

[3] M. Millot, N. Dubrovinskaia, A. Cernok, S. Blaha, L. Dubrovinsky, D. G. Braun, P. M. Celliers, G. W. Collins, J. H. Eggert, and R. Jeanloz, Science **347**, 418 (2015).

[4] A. J. MacKinnon, N. B. Meezan, J. S. Ross, S. Le Pape, L. Berzak Hopkins, L. Divol, D. Ho, J. Milovich, A. Pak, J. Ralph, T. Döppner, P. K. Patel, C. Thomas, R. Tommasini, S. Haan, A. G. MacPhee, J. McNaney, J. Caggiano, R. Hatarik, R. Bionta *et al.*, Phys. Plasmas **21**, 056318 (2014).

[5] J. S. Ross, D. Ho, J. Milovich, T. Döppner, J. McNaney, A. G. MacPhee, A. Hamza, J. Biener, H. F. Robey, E. L. Dewald, R. Tommasini, L. Divol, S. Le Pape, L. B. Hopkins, P. M. Celliers, O. Landen, N. B. Meezan, and A. J. Mackinnon, Phys. Rev. E **91**, 021101 (2015).

[6] L. F. Berzak Hopkins, N. B. Meezan, S. Le Pape, L. Divol, A. J. Mackinnon, D. D. Ho, M. Hohenberger, O. S. Jones, G. Kyrala, J. L. Milovich, A. Pak, J. E. Ralph, J. S. Ross, L. R. Benedetti, J. Biener, R. Bionta, E. Bond, D. Bradley, J. Caggiano, D. Callahan *et al.*, Phys. Rev. Lett. **114**, 175001 (2015).

[7] N. B. Meezan, L. F. Berzak Hopkins, S. Le Pape, L. Divol, A. J. MacKinnon, T. Döppner, D. D. Ho, O. S. Jones, S. F. Khan, T. Ma, J. L. Milovich, A. E. Pak, J. S. Ross, C. A. Thomas, L. R. Benedetti, D. K. Bradley, P. M. Celliers, D. S. Clark, J. E. Field, S. W. Haan *et al.*, Phys. Plasmas **22**, 062703 (2015).

[8] L. F. Berzak Hopkins, S. Le Pape, L. Divol, N. B. Meezan, A. J. Mackinnon, D. D. Ho, O. S. Jones, S. Khan, J. L. Milovich, J. S. Ross, P. Amendt, D. Casey, P. M. Celliers, A. Pak, J. L. Peterson, J. Ralph, and J. R. Rygg, Phys. Plasmas **22**, 056318 (2015).

[9] S. L. Pape, L. F. B. Hopkins, L. Divol, A. Pak, E. Dewald, N. B. Meezan, D. D.-m. Ho, S. F. Khan, A. J. Mackinnon, C. Weber, C. Goyon, J. S. Ross, M. Millot, L. R. Bennedetti, N. Izumi, G. A. Kyrala, T. Ma, S. R. Nagel, D. Edgell, A. G. Macphee *et al.* (unpublished).

[10] H. Nagao, K. G. Nakamura, K. Kondo, N. Ozaki, K. Takamatsu, T. Ono, T. Shiota, D. Ichinose, K. A. Tanaka, K. Wakabayashi, K. Okada, M. Yoshida, M. Nakai, K. Nagai, K. Shigemori, T. Sakaiya, and K. Otani, Phys. Plasmas **13**, 052705 (2006).

[11] S. Brygoo, E. Henry, P. Loubeyre, J. Eggert, M. Koenig, B. Loupias, A. Benuzzi-Mounaix, and M. Rabec Le Gloahec, Nat. Mater. **6**, 274 (2007).

[12] D. G. Hicks, T. R. Boehly, P. M. Celliers, D. K. Bradley, J. H. Eggert, R. S. McWilliams, R. Jeanloz, and G. W. Collins, Phys. Rev. B **78**, 174102 (2008).

[13] M. D. Knudson, M. P. Desjarlais, and D. H. Dolan, Science **322**, 1822 (2008).

[14] R. S. McWilliams, J. H. Eggert, D. G. Hicks, D. K. Bradley, P. M. Celliers, D. K. Spaulding, T. R. Boehly, G. W. Collins, and R. Jeanloz, Phys. Rev. B **81**, 014111 (2010).

[15] M. C. Gregor, D. E. Fratanduono, C. A. McCoy, D. N. Polsin, A. Sorce, J. R. Rygg, G. W. Collins, T. Braun, P. M. Celliers, J. H. Eggert, D. D. Meyerhofer, and T. R. Boehly, Phys. Rev. B **95**, 144114 (2017).

[16] D. K. Bradley, J. H. Eggert, R. F. Smith, S. T. Prisbrey, D. G. Hicks, D. G. Braun, J. Biener, A. V. Hamza, R. E. Rudd, and G. W. Collins, Phys. Rev. Lett. **102**, 075503 (2009).

[17] R. F. Smith, J. H. Eggert, R. Jeanloz, T. S. Duffy, D. G. Braun, J. R. Patterson, R. E. Rudd, J. Biener, A. E. Lazicki, A. V. Hamza, J. Wang, T. Braun, L. X. Benedict, P. M. Celliers, and G. W. Collins, Nature (London) **511**, 330 (2014).

[18] D. K. Bradley, J. H. Eggert, D. G. Hicks, P. M. Celliers, S. J. Moon, R. C. Cauble, and G. W. Collins, Phys. Rev. Lett. **93**, 195506 (2004).

[19] J. H. Eggert, D. G. Hicks, P. M. Celliers, D. K. Bradley, R. S. McWilliams, R. Jeanloz, J. E. Miller, T. R. Boehly, and G. W. Collins, Nat. Phys. **6**, 40 (2009).

[20] J. Biener, D. Ho, A. Hamza, and E. Al, Nucl. Fusion **49**, 112001 (2009).

[21] C. Dawedeit, S. O. Kucheyev, S. J. Shin, T. M. Willey, M. Bagge-Hansen, T. Braun, Y. M. Wang, B. S. El-Dasher, N. E. Teslich, M. M. Biener, J. Ye, L. Kirste, C.-C. C. Roehlig, M. Wolfer, E. Woerner, A. W. van Buuren, A. V. Hamza, C. Wild, and J. Biener, Diamond Relat. Mater. **40**, 75 (2013).

[22] H. F. Robey, P. M. Celliers, J. L. Kline, A. J. Mackinnon, T. R. Boehly, O. L. Landen, J. H. Eggert, D. Hicks, S. Le Pape, D. R. Farley, M. W. Bowers, K. G. Krauter, D. H. Munro, O. S. Jones, J. L. Milovich, D. Clark, B. K. Spears, R. P. J. Town, S. W. Haan, S. Dixit *et al.*, Phys. Rev. Lett. **108**, 215004 (2012).

[23] H. F. Robey, T. R. Boehly, P. M. Celliers, J. H. Eggert, D. Hicks, R. F. Smith, R. Collins, M. W. Bowers, K. G. Krauter, P. S. Datte, D. H. Munro, J. L. Milovich, O. S. Jones, P. A. Michel, C. A. Thomas, R. E. Olson, S. Pollaine, R. P. J. Town, S. Haan, D. Callahan *et al.*, Phys. Plasmas **19**, 042706 (2012).

[24] S. Hamel, L. Benedict, P. Celliers, M. Barrios, T. Boehly, G. Collins, T. Döppner, J. Eggert, D. Farley, D. Hicks, J. Kline, A. Lazicki, S. LePape, A. Mackinnon, J. Moody, H. Robey, E. Schwegler, and P. Sterne, Phys. Rev. B **86**, 094113 (2012).

[25] J. D. Moody, H. F. Robey, P. M. Celliers, D. H. Munro, D. A. Barker, K. L. Baker, T. Döppner, N. L. Hash, L. Berzak Hopkins, K. LaFortune, O. L. Landen, S. LePape, B. J. MacGowan, J. E. Ralph, J. S. Ross, C. Widmayer, A. Nikroo, E. Giraldez, and T. Boehly, Phys. Plasmas **21**, 092702 (2014).

[26] H. F. Robey, P. M. Celliers, J. D. Moody, J. Sater, T. Parham, B. Kozioziemski, R. Dylla-Spears, J. S. Ross, S. LePape, J. E. Ralph, M. Hohenberger, E. L. Dewald, L. Berzak Hopkins, J. J. Kroll, B. E. Yoxall, A. V. Hamza, T. R. Boehly, A. Nikroo, O. L. Landen, and M. J. Edwards, Phys. Plasmas **21**, 022703 (2014).

[27] P. M. Celliers, D. K. Bradley, G. W. Collins, D. G. Hicks, T. R. Boehly, and W. J. Armstrong, Rev. Sci. Instrum. **75**, 4916 (2004).

[28] A. Pak, L. Divol, A. L. Kritcher, T. Ma, J. E. Ralph, B. Bachmann, L. R. Benedetti, D. T. Casey, P. M. Celliers, E. L. Dewald, T. Döppner, J. E. Field, D. E. Fratanduono, L. F. Berzak Hopkins, N. Izumi, S. F. Khan, O. L. Landen, G. A. Kyrala, S. LePape, M. Millot *et al.*, Phys. Plasmas **24**, 056306 (2017).

[29] L. Divol, A. Pak, L. F. Berzak Hopkins, S. Le Pape, N. B. Meezan, E. L. Dewald, D. D.-M. Ho, S. F. Khan, A. J. Mackinnon, J. S. Ross, D. P. Turnbull, C. Weber, P. M. Celliers, M. Millot, L. R. Benedetti, J. E. Field, N. Izumi, G. A. Kyrala, T. Ma, S. R. Nagel *et al.*, Phys. Plasmas **24**, 056309 (2017).

[30] E. L. Dewald, F. Hartemann, P. Michel, J. Milovich, M. Hohenberger, A. Pak, O. L. Landen, L. Divol, H. F. Robey, O. A. Hurricane, T. Döppner, F. Albert, B. Bachmann, N. B. Meezan, A. J. Mackinnon, D. Callahan, and M. J. Edwards, Phys. Rev. Lett. **116**, 075003 (2016).

[31] M. D. Knudson and M. P. Desjarlais, Phys. Rev. B **88**, 184107 (2013).

[32] G. I. Kerley, Equations of state for hydrogen and deuterium, Sandia National Laboratories Technical Report No. SAND2003-3613, 2003, doi:10.2172/917468.

[33] L. Caillabet, S. Mazevet, and P. Loubeyre, Phys. Rev. B **83**, 094101 (2011).

[34] P. M. Celliers, G. W. Collins, D. G. Hicks, and J. H. Eggert, J. Appl. Phys. **98**, 113529 (2005).

[35] S. Brygoo, M. Millot, P. Loubeyre, A. E. Lazicki, S. Hamel, T. Qi, P. M. Celliers, F. Coppari, J. H. Eggert, D. E. Fratanduono, D. G. Hicks, J. R. Rygg, R. F. Smith, D. C. Swift, G. W. Collins, and R. Jeanloz, J. Appl. Phys. **118**, 195901 (2015).

[36] L. X. Benedict, K. P. Driver, S. Hamel, B. Militzer, T. Qi, A. A. Correa, A. Saul, and E. Schwegler, Phys. Rev. B **89**, 224109 (2014).

[37] D. G. Hicks, T. R. Boehly, P. M. Celliers, J. H. Eggert, S. J. Moon, D. D. Meyerhofer, and G. W. Collins, Phys. Rev. B **79**, 014112 (2009).

[38] P. Loubeyre, S. Brygoo, J. Eggert, P. M. Celliers, D. K. Spaulding, J. R. Rygg, T. R. Boehly, G. W. Collins, and R. Jeanloz, Phys. Rev. B **86**, 144115 (2012).

[39] M. D. Knudson and M. P. Desjarlais, Phys. Rev. Lett. **118**, 035501 (2017).

[40] A. A. Correa, S. A. Bonev, and G. Galli, Proc. Natl. Acad. Sci. USA **103**, 1204 (2006).

[41] Z. G. Hu and P. Hess, Appl. Phys. Lett. **89**, 081906 (2006).

[42] F. Klauser, D. Steinmuller-Nethl, R. Kaindl, E. Bertel, and N. Memmel, Chem. Vap. Deposition **16**, 127 (2010).

[43] S. Potocky, A. Kromka, J. Potmesil, Z. Remes, Z. Polackova, and M. Vanecek, Phys. Status Solidi A **203**, 3011 (2006).

[44] Z. G. Hu, P. Prunici, P. Hess, and K. H. Chen, J. Mater. Sci.: Mater. Electron. **18**, 37 (2007).

[45] T. Ruf, M. Cardona, C. S. J. Pickles, and R. Sussmann, Phys. Rev. B **62**, 16578 (2000).

[46] J. Fontanella, R. L. Johnston, J. H. Colwell, and C. Andeen, Appl. Opt. **16**, 2949 (1977).

[47] W. Theobald, J. E. Miller, T. R. Boehly, E. Vianello, D. D. Meyerhofer, T. C. Sangster, J. Eggert, and P. M. Celliers, Phys. Plasmas **13**, 122702 (2006).
[48] A. A. Correa, L. X. Benedict, D. A. Young, E. Schwegler, and S. A. Bonev, Phys. Rev. B **78**, 024101 (2008).
[49] G. I. Kerley and L. C. Chhabuldas, Multicomponent-multiphase equation of state for carbon, Sandia National Laboratories Technical Report No. SAND2001-2619, 2001, doi:10.2172/787608
[50] J. R. Rygg (unpublished).
[51] F. Peter, Z. Phys. **15**, 358 (1923).
[52] G. Ghosh, Opt. Commun. **163**, 95 (1999).